Check for updates

High-efficiency thermoelectric $Ba_8Cu_{14}Ge_6P_{26}$: bridging the gap between tetrel-based and tetrel-free clathrates†

Jian Wang, [ab] Oleg I. Lebedev, [c] Kathleen Lee, [bd] Juli-Anna Dolyniuk, [b] Peter Klavins, [e] Sabah Bux [d] and Kirill Kovnir ⋆[abf]

A new type-I clathrate, $Ba_8Cu_{14}Ge_6P_{26}$, was synthesized by solid-state methods as a polycrystalline powder and grown as a cm-sized single crystal *via* the vertical Bridgman method. Single-crystal and powder X-ray diffraction show that $Ba_8Cu_{14}Ge_6P_{26}$ crystallizes in the cubic space group $Pm\bar{3}n$ (no. 223). $Ba_8Cu_{14}Ge_6P_{26}$ is the first representative of anionic clathrates whose framework is composed of three atom types of very different chemical natures: a transition metal, tetrel element, and pnicogen. Uniform distribution of the Cu, Ge, and P atoms over the framework sites and the absence of any superstructural or local ordering in $Ba_8Cu_{14}Ge_6P_{26}$ were confirmed by synchrotron X-ray diffraction, electron diffraction and high-angle annular dark field scanning transmission electron microscopy, and neutron and X-ray pair distribution function analyses. Characterization of the transport properties demonstrate that $Ba_8Cu_{14}Ge_6P_{26}$ is a p-type semiconductor with an intrinsically low thermal conductivity of 0.72 W m^{-1} K^{-1} at 812 K. The thermoelectric figure of merit, ZT, for a slice of the Bridgman-grown crystal of $Ba_8Cu_{14}Ge_6P_{26}$ approaches 0.63 at 812 K due to a high power factor of 5.62 μW cm^{-1} K^{-2}. The thermoelectric efficiency of $Ba_8Cu_{14}Ge_6P_{26}$ is on par with the best optimized p-type Ge-based clathrates and outperforms the majority of clathrates in the 700–850 K temperature region, including all tetrel-free clathrates. $Ba_8Cu_{14}Ge_6P_{26}$ expands clathrate chemistry by bridging conventional tetrel-based and tetrel-free clathrates. Advanced transport properties, in combination with earth-abundant framework elements and congruent melting make $Ba_8Cu_{14}Ge_6P_{26}$ a strong candidate as a novel and efficient thermoelectric material.

Introduction

Thermoelectric materials play an important role in renewable energy applications, which can convert waste heat into electrical energy and *vice versa*.[1–3] The efficiency of thermoelectric materials is characterized by the dimensionless figure of merit, $ZT = S^2T/\rho\kappa$, where S is the Seebeck thermopower, T is the absolute temperature, ρ is the electrical resistivity, and κ is the thermal conductivity. In crystalline solids, the intrinsic correlations between these three transport properties make enhancement of thermoelectric

efficiency challenging due to their dependence on carrier concentration and electronic structure.[4–9] The Phonon Glass-Electron Crystal (PGEC) concept was proposed as a way to guide thermoelectric research.[10–13] Clathrate compounds, also known as host–guest compounds, are considered to be PGEC compounds due to their covalent three-dimensional frameworks and rattling of guest atoms. The framework acts as a good electrical conductor, while the rattling of guest atoms encapsulated in the framework cages efficiently scatters phonons to reduce thermal conductivity.[12,14–23] Besides thermoelectric applications, clathrates are used as photovoltaic materials, Li-batteries anodes, superconductors, and gas storage materials.[16,17]

Based on the framework-forming elements, all anionic clathrates can be divided into two main groups: tetrel-based (Si, Ge, Sn) and tetrel-free clathrates. The latter group, which is much smaller than the former one, can also be called pnicogen-based or transition metal-based clathrates since the frameworks of all reported tetrel-free clathrates are formed by a combination of the late transition metals of group 10–12 with pnicogen atoms: P, As, or Sb.[17] Both groups have distinct chemical and structural properties. One specific feature of tetrel clathrates is the formation of locally disordered frameworks where one crystallographic position is jointly occupied by different atoms,

[a]Department of Chemistry, Iowa State University, Ames, Iowa 50011, USA

[b]Department of Chemistry, University of California, Davis, CA 95616, USA. E-mail: kovnir@iastate.edu

[c]Laboratoire CRISMAT, ENSICAEN, CNRS, UMR 6508, F-14050 Caen, France

[d]Thermal Energy Conversion Research and Advancement Group, Jet Propulsion Laboratory, Pasadena, CA 91109, USA

[e]Department of Physics, University of California, Davis, CA 95616, USA

[f]Ames Laboratory, Iowa State University, Ames, Iowa 50011, USA

such as Ga/Ge or Zn/Sn.[16,17] In turn, tetrel-free clathrates show full segregation of transition metal and phosphorus atoms over different framework positions, which result in the formation of either long-range ordered structures, as in the case of $Ba_8M_{16}P_{30}$, BaM_2P_4, and $Ba_8Zn_{11}Cu_{13}P_{28+\delta}$ (M = Cu, Au, Ni), or short-range ordering, as in the case of $Ba_8(Cu/Zn)_{16+y}P_{30-y}$.[15,18,24–26]

In this work, we report a new type-I clathrate, $Ba_8Cu_{14}Ge_6P_{26}$, which combines a transition metal, tetrel element, and pnicogen in its framework. This compound was synthesized and grown as a large crystal through the Bridgman technique. A uniform distribution of the constituent elements and the absence of short- or long-range ordering in the $Ba_8Cu_{14}Ge_6P_{26}$ clathrate was confirmed by a combination of synchrotron powder X-ray diffraction, high-angle annular dark field scanning transmission electron microscopy, and X-ray and neutron pair distribution function analyses. Thermoelectric measurements demonstrate that $Ba_8Cu_{14}Ge_6P_{26}$ is a p-type semiconductor with a remarkable figure of merit. This newly discovered clathrate builds a bridge between the two clathrate families.

Experimental section

Synthesis

All preparation and handling of samples were performed in an argon-filled glovebox with the O_2 level below 1 ppm. All starting materials were commercial grade and were used as received: Ba chunks (Sigma-Aldrich, 99.9%), Cu powder (Sigma-Aldrich, 99.9%), Ge pieces (Alfa Aesar, 99.9999%) and red P powder (Alfa Aesar, 99%).

The polycrystalline sample of $Ba_8Cu_{14}Ge_6P_{26}$ was obtained *via* the solid-state reaction of the elements. The elements with a stoichiometric Ba/Cu/Ge/P ratio of 8/14/6/26 were loaded into a carbonized silica ampoule, evacuated, and flame-sealed. The ampoule was first heated from room temperature to 1123 K over 17 h, and then it was annealed at this temperature for 144 hours. After the furnace was turned off and cooled, the samples were ground and reloaded into a new carbonized silica ampoule in the glovebox, resealed, and reannealed using the same temperature profile as the first annealing. The same procedure was repeated a third time. After three annealings, a uniform melted chunk was found as the final product, and was characterized as single-phase by powder X-ray diffraction (Fig. 1 and S1†).

Differential scanning calorimetry

A Netzsch Differential Scanning Calorimeter (DSC) was used to characterize the thermal behavior of $Ba_8Cu_{14}Ge_6P_{26}$. A powder sample (mass: 35.3 mg) was sealed inside an evacuated silica ampoule, heated to 1273 K and cooled down to room temperature with the 10 K min^{-1} rate.

Bridgman growth

About 5 g of single-phase polycrystalline sample was ground into fine powder in a mortar and loaded into a carbonized silica ampoules with a sharp cone end. The ampoule was evacuated
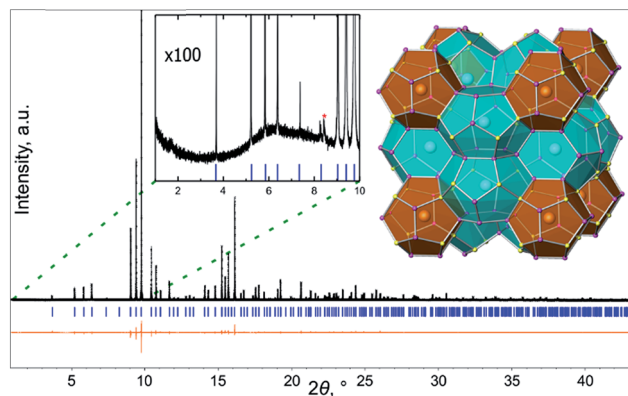

Fig. 1 Results of Rietveld refinement of the synchrotron powder X-ray diffraction data of $Ba_8Cu_{14}Ge_6P_{26}$. Experimental pattern: black crosses; calculated pattern: black line; calculated peak positions: blue sticks; difference curve: orange line. Left inset: enhanced view of the low angle part of the experimental pattern with the calculated peak positions shown as blue sticks. One admixture peak is indicated with red star. Right inset: general view of the crystal structure with two types of polyhedra highlighted in (pentagonal dodecahedra) brown and (tetrakaidecahedra) cyan.

and flame-sealed. This ampoule was further sealed in another thick-walled silica ampoule, which was used to protect the growth tube. The silica ampoule was placed into a home-made two-zone vertical Bridgman furnace for crystal growth. An "oscillating" temperature profile was first applied to melt the sample thoroughly. When the ampoule was placed in the hot zone, the temperature in the hot zone was set to 1208(5) K for 24 hours, then cooled down to 973(5) K for 12 hours and afterwards the temperature was increased to 1123(5) K for 120 hours. After the melt process, the ampoule was dropped at a rate of 2.3 mm h^{-1} from the hot zone to the cold zone, where the temperature in the hot zone was 1123(5) K, and the temperature of the cold zone was 973(5) K. The crystal growth was completed in five days. Several crystals were grown to check for reproducibility. The Archimedean densities of the crystal slices vary in the range of 99.4–99.8% from theoretical X-ray density.

Elemental analysis

Elemental analysis of selected crystals was carried out on a Hitachi S4100T scanning electron microscope (SEM) with energy-dispersive X-ray (EDX) microanalysis (Oxford INCA Energy) to check for a consistent elemental ratio of the elements in the samples (Fig. S3 and Table S3†).

Single-crystal X-ray diffraction

Single-crystal diffraction experiments were collected at 90 K using a Bruker AXS SMART diffractometer with an APEX-II CCD detector with Mo-K$_\alpha$ radiation. The datasets were recorded as ω-scans with a 0.4° step width and integrated with the Bruker SAINT software package.[27] Multi-scan absorption corrections were applied.[27] The solution and refinement of the crystal structure were carried out using the SHELX-2014 suite of programs.[28] The final refinements were performed using

anisotropic atomic displacement parameters for all atoms. A summary of pertinent information relating to unit cell parameters, data collection, and refinements is provided in Table 1 and the atomic parameters and interatomic distances are provided in Tables S1 and S2.† Further details of the crystal structure determination may be obtained from Fachinformationszentrum Karlsruhe, Germany, by quoting the depository number CSD-433052.

Transmission electron microscopy (TEM)

Samples for electron microscopy were ground under ethanol, and the resulting dispersion was transferred to a holey carbon film fixed on a 3 mm copper grid. Electron diffraction (ED) studies were performed using a Tecnai G2 30 UT (LaB_6) microscope operated at 300 kV with 0.17 nm point resolution. High-angle annular dark field (HAADF)-scanning TEM (STEM) studies and EDX elemental mapping were performed using a JEM ARM200F cold FEG double aberration corrected electron microscope operated at 200 kV and equipped with a large solid-angle CENTURIO EDX detector and Quantum EELS spectrometer.

X-ray and neutron powder diffraction and PDF

All samples were characterized by X-ray powder diffraction (XRD) using a Rigaku Miniflex 600 diffractometer employing Cu-K_α radiation. High-resolution room temperature synchrotron powder XRD data were collected at beamline 11-BM ($\lambda = 0.459266$ Å) at the Advanced Photon Source (APS) at Argonne National Laboratory (ANL) (Fig. 1). The refined unit cell parameter of $Ba_8Cu_{14}Ge_6P_{26}$ from synchrotron X-ray diffraction data at room temperature, $a = 10.09454(1)$ Å, agrees with the result obtained from single-crystal refinement, $a = 10.0626(8)$ Å at 90 K. Neutron powder diffraction time-of-flight data for neutron pair distribution function (N-PDF) were collected at the NOMAD beamline at the Spallation Neutron Source (SNS) at Oak Ridge National Laboratory (ORNL). Additional high-energy total X-ray scattering (X-PDF) data ($\lambda = 0.21$ Å) were collected at the PDF beamline 11-ID-B at APS ANL. Neutron and X-ray PDF data were analyzed using PDFGUI.[29,30]

Table 1 Selected single crystal data and structure refinement parameters for $Ba_8Cu_{14}Ge_6P_{26}$

Temperature	90(2) K
Radiation, wavelength	Mo-K_α, 0.71073 Å
Space group	$Pm\bar{3}n$ (no. 223)
Unit cell dimensions	$a = 10.0626(8)$ Å
Unit cell volume, Z	1018.9(2) Å^3, 1
Density (calc.)	5.26 g cm^{-3}
Absorption coefficient	19.61 cm^{-1}
Data/parameters	333/25
Goodness-of-fit	1.14
Final R indices [$I > 2\sigma(I)$]	$R_1 = 0.015$
	$wR_2 = 0.025$
Final R indices [all data]	$R_1 = 0.017$
	$wR_2 = 0.026$
Max diff. peak and hole	0.80 and -0.53

Transport properties

Transport properties were studied on several slices of different Bridgman-grown crystals. Low-temperature transport properties in the temperature range of 2–400 K were studied using the commercial multipurpose Physical Properties Measurement System (PPMS, Quantum Design). The Seebeck thermopower and thermal conductivity were measured using the thermal transport option. The electrical resistivity was measured by a standard four-point alternating-current technique to exclude the resistance of the leads. High-temperature thermal conductivity was carried on a Netzsch LFA 457. The Seebeck coefficient and resistivity measurements were conducted simultaneously on a Linseis LSR-3/1100 instrument system under helium atmosphere. The high-temperature data were additionally verified at the Jet Propulsion Laboratory using both custom and commercial apparatus. The Seebeck coefficient was measured using the light-pipe method with tungsten–niobium thermocouples under high vacuum in a custom set-up.[31] Temperature-dependent resistivity was measured using a Van der Pauw 4-point method with tungsten pressure contact probes.[32] Thermal diffusivity was measured using a Netzsch LFA 404 system. The temperature was limited to 800 K to prevent sublimation of the samples during measurements. All transport measurements were taken during both heating and cooling (heating rate of 180 K h^{-1}), and showed no hysteresis. The combined measurement uncertainty in the thermoelectric figure of merit is generally assumed to be ~20%.

Results and discussion

Composition and crystal structure

Our motivation to search for new clathrates was to produce electron-balanced compounds with the semiconductor-like properties that are highly desirable for thermoelectric applications. The clathrate $Ba_8Cu_{16}P_{30}$ was reported to exhibit metallic properties due to an insufficient number of valence electrons to form four bonds per clathrate framework atom.[25,33,34] In this work we realized an electron-balanced compound by the replacement of some Cu (1 valence electron) and P (5 valence electrons) atoms with Ge (4 valence electrons) atoms. Several synthesized samples with different nominal Ba/Ge/Cu/P ratios contained the same phase with a similar composition as was evidenced by EDX and unit cell parameter determinations. The precise elemental ratio in the new clathrate was determined by a combination of three different methods. First, the refinement of single-crystal X-ray diffraction data resulted in the chemical formula of $Ba_8M_{20.1(2)}P_{25.9(2)}$, where M indicates the merging of Cu and Ge elements due to their similar X-ray atomic scattering factors. Tests of different crystals selected from different batches all resulted in an identical composition within the standard deviations of the refinements. Afterwards, the chemical composition of different crystals analyzed by EDX spectroscopy resulted in the formula $Ba_8Cu_{14.4(2)}Ge_{5.5(1)}P_{22(1)}$ when normalized to 8 Ba atoms (Table S3†). Note that light P atoms cannot be accurately determined by EDX, and some overlap of Cu and Ge lines hinder precise determination of the elemental

contents. However, the averaged amount of Cu + Ge from EDX is 19.9(3), which agrees very well with the results from single-crystal diffraction. Finally, Zintl counting exactly predicts the $Ba_8Cu_{14}Ge_6P_{26}$ composition for 20 metal Cu + Ge atoms. Indeed, in the clathrate-I system Ba_8X_{46}, where X is the framework atom, each Ba atoms donates 2 electrons to the framework becoming Ba^{2+}, and 4 electrons are required for per framework atom, X, to achieve an electron balance by forming 4 covalent bonds in the framework.[17] Since there are 46 atoms in the framework, a total of $46 \times 4 = 184$ electrons are required. Besides the 16 electrons from Ba atoms, the framework atoms need additional 168 electrons coming from X elements. Assuming the total Cu + Ge content is equal to 20 and 26 P atoms in the framework, the only electron-balanced solution is 14 Cu atoms ($14 \times 1 = 14$ electrons), 6 Ge atoms ($6 \times 4 = 24$ electrons), and 26 P atoms ($26 \times 5 = 130$ electrons), resulting in exactly 168 electrons. The electron-balanced nature of $Ba_8Cu_{14}Ge_6P_{26}$ was further confirmed by properties measurements (*vide infra*). All our attempts to synthesize samples with $Ba_8Cu_{14+x}Ge_{6-x}P_{26}$ nominal compositions, where x varies from 0.1 to 1, resulted in no detectable unit cell parameter shifts or changes in transport properties, indicating that $Ba_8Cu_{14}Ge_6P_{26}$ is a line compound.

$Ba_8Cu_{14}Ge_6P_{26}$ crystallizes in the clathrate-I structure type with the space group $Pm\bar{3}n$ (no. 223). Clathrate-I is the most abundant structure type among inorganic clathrates. Its crystal structure can be described as composed of two types of polyhedra: pentagonal dodecahedra and tetrakaidecahedra. The Ba atoms are encapsulated inside both types of polyhedra. Tetrakaidecahedra share their hexagonal faces, forming columns running along all three main crystallographic directions and the residual space filled by dodecahedra (Fig. 1 inset). There is no evidence for vacancies on the Ba sites. Three framework sites, 6c, 16i, and 24k are jointly occupied by Cu, Ge and P. Cu and Ge, atomic numbers 29 and 32, are difficult to distinguish by X-ray diffraction due to similar atomic scattering factors. During the refinement, all framework sites were originally refined as jointly occupied by Cu and P under the constraints of equivalent atomic displacement parameters and the total occupancy of each site was fixed to 100%. Similar refinements with all framework positions set as Ge/P resulted in a slightly lower but similar M/P ratio. At the final stages of the refinement, each framework site was refined as jointly occupied by Cu + Ge + P. An additional compositional restraint was applied to fix the total elemental content in the structure to 14Cu + 6Ge + 26P (Tables 1, S1, and S2†). Mixed occupancy of the framework positions by several different elements, including Cu/Ge mixing, is common for the tetrel clathrates, such as $Ba_8Ga_{16}Ge_{30}$,[35] $Ba_8Ga_{17.1}Ge_{25.6}Sb_{2.7}$,[36] and $Ba_8Cu_{6-x}Ge_{40+x}$.[37]

Superstructures and partial orderings are well-known in the crystal chemistry of clathrates. For the type-I clathrate, the aristotype structure crystallizes in space group $Pm\bar{3}n$ (no. 223) with $a \approx 10$ Å and volume $V \approx 1000$ Å^3. Different kinds of superstructures have been reported for type-I clathrates ranging from lowered symmetry within the same volume unit cell[38] to an increase of the unit cell volume by a factor of 4–8 due to either the ordering of vacancies in the tetrel-based clathrates, as in the

cases of Cs_8Sn_{44} or Ba_8Ge_{43}, or the separation of atoms of different chemical natures over distinct framework sites, as in the case of $Ba_8Cu_{16}P_{30}$ and $Ba_8Au_{16}P_{30}$.[15,24,39–41] The vacancies in the framework or guest positions do not necessarily lead to the formation of a superstructure.[42,43] Alternatively, the formation of short-range ordering without a long-range superstructure is possible, but is more difficult to detect with diffraction techniques and requires the application of local probes. For example, the recently reported type-I clathrate $Ba_8M_{16+y}P_{30-y}$ (M = Cu, Zn) exhibits partial superstructural ordering confirmed with ED, STEM, and PDF, and can also be detected due to presence of weak extra diffraction peaks in its synchrotron powder diffraction pattern.[25] No such extra peaks were detected in the diffraction pattern of $Ba_8Cu_{14}Ge_6P_{26}$ sample (Fig. 1 inset), which demonstrates the absence of long-range superstructural ordering in $Ba_8Cu_{14}Ge_6P_{26}$. To further investigate possible short-range ordering, we applied electron microscopy.

Elemental mapping shows uniform distributions of the Ba, Cu, Ge, and P elements over the entire studied crystals (Fig. 2b). All observed diffraction spots in the ED patterns can be indexed in the cubic clathrate-I unit cell. No superstructural reflections were found (Fig. 2a). This is in a stark contrast to the $Ba_8M_{16+y}P_{30-y}$ (M = Cu, Zn) clathrate where preferential Cu–Zn bonding resulted in the formation of a trigonal superstructure, detectable by ED.[25] High-resolution HAADF–STEM investigations confirm the well-ordered cubic nature of the
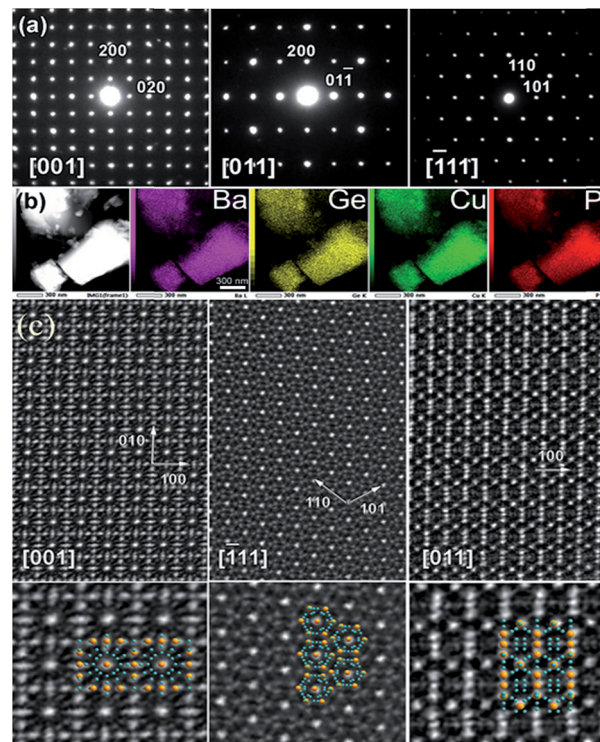

Fig. 2 (a) ED patterns along the main cubic zones and (b) elemental mapping of selected $Ba_8Cu_{14}Ge_6P_{26}$ crystals. Ba: purple, Ge: yellow, Cu: green, P: red. (c) HAADF–STEM images along main zone axes [001], [$\bar{1}$11] and [011] of $Ba_8Cu_{14}Ge_6P_{26}$ are shown. The insets in the bottom show structural fragment overlaps (Ba: yellow, Cu/Ge/P: blue).

$Ba_8Cu_{14}Ge_6P_{26}$ crystallites with good agreement to the overlayed structural models (Fig. 2c). No structural defects, like antiphase boundaries or stacking faults, were observed in the studied $Ba_8Cu_{14}Ge_6P_{26}$ crystallites.

Synchrotron X-ray and neutron PDF analyses also confirmed the absence of local ordering in $Ba_8Cu_{14}Ge_6P_{26}$ (Fig. 3). Independent fittings of the short-range (1.9 Å ≤ r ≤ 9.9 Å) and long range (9.9 Å ≤ r ≤ 19.9 Å) PDF regions were performed using the cubic $Pm\bar{3}n$ model. Due to the similarity of the neutron scattering lengths for Cu (7.7 fm) and Ge (8.2 fm) the occupancies of the atomic positions in the framework were fixed to the values obtained from the single crystal X-ray diffraction experiment and were not refined further. The structural model determined from the single crystal X-ray experiment describes the PDF patterns well, indicating the absence of any short-range ordering. The presence of local ordering in the clathrate framework results in significant perturbations of the short-range PDF data.[25]

Based on TEM, synchrotron XRD, and PDF results, the crystal structure of $Ba_8Cu_{14}Ge_6P_{26}$ is established to have primitive cubic $Pm\bar{3}n$ symmetry with a uniform distribution of the framework elements and without local ordering, superstructure, or defects. The main difference between the Cu–Zn–P and Cu–Ge–P frameworks is the preference for Cu and Zn to form chemical bonds to each other. We have elegantly shown that an increase of the Zn content resulted in the formation of a clathrate where all metal atoms are joined in Cu–Zn dumbbells.[26] Apparently, such bonding preference is absent in the case of the Ba–Cu–Ge–P clathrate, which resulted in the formation of the cubic structure with a uniform distribution of Cu, Ge, and P over the clathrate framework sites.

Although clathrate-I is a well-known structure type, $Ba_8Cu_{14}Ge_6P_{26}$ is the first representative of inorganic clathrates with electropositive guest atoms where the framework is composed of a transition metal, tetrel element, and pnicogen. The tetrel-based clathrates are a prevailing group with over 100 compounds with diverse properties.[17] Until now, only a dozen tetrel-free clathrates have been reported, which include phosphides, $Ba_8M_{16}P_{30}$ (ref. 15 and 24) and AeM_2P_4 (Ae = Sr, Ba; M = Ni, Cu),[18] arsenides and antimonides, $A_8E_{18}Pn_{28}$, A = Rb, Cs; E = Zn, Cd; Pn = As, Sb.[44,45] Prior to our work, there was an insurmountable gap between these two clathrate groups, despite the reported attempts to dope Sb into tetrel clathrates.[36] $Ba_8Cu_{14}Ge_6P_{26}$ fills the gap between tetrel-based and pnicogen-based clathrates and provides new insight and opportunities for clathrate research. High thermal stability and the electron-balanced nature of this clathrate result in outstanding transport properties.

Thermal stability

DSC characterization results for $Ba_8Cu_{14}Ge_6P_{26}$ are shown in Fig. 4 and S4.† $Ba_8Cu_{14}Ge_6P_{26}$ melts congruently at 1108(3) K and recrystallizes at 1006(3) K. No decomposition or phase transition were detected upon melting and crystallization, which was verified by powder XRD (Fig. S2†). The thermal stability of $Ba_8Cu_{14}Ge_6P_{26}$ was further confirmed by powder XRD of the phase after annealing a single-phase sample in a sealed tube at 1223 K for 12 hours. The congruent melting of $Ba_8Cu_{14}Ge_6P_{26}$ makes the single-crystal growth process feasible. We applied the vertical Bridgman method to grow large crystals of $Ba_8Cu_{14}Ge_6P_{26}$ (Fig. 4 bottom inset). A slice of the grown crystal with a mirror-like surface is also shown in Fig. 4 top inset.

Thermoelectric properties

The presence of grain boundaries may mask the intrinsic properties of solids. In thermoelectric characterization of
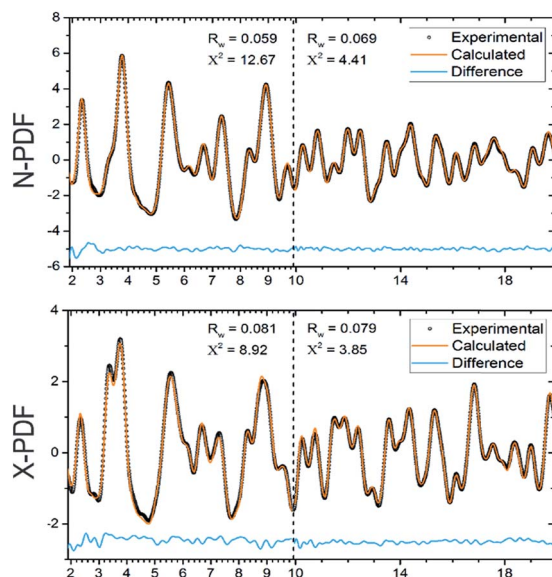

Fig. 3 Experimental neutron (top) and X-ray (bottom) pair distribution functions and their fits are shown for a cubic model of $Ba_8Cu_{14}Ge_6P_{26}$. Experimental data are open black circles, calculated fits are red lines, and difference curves are shown as blue lines.
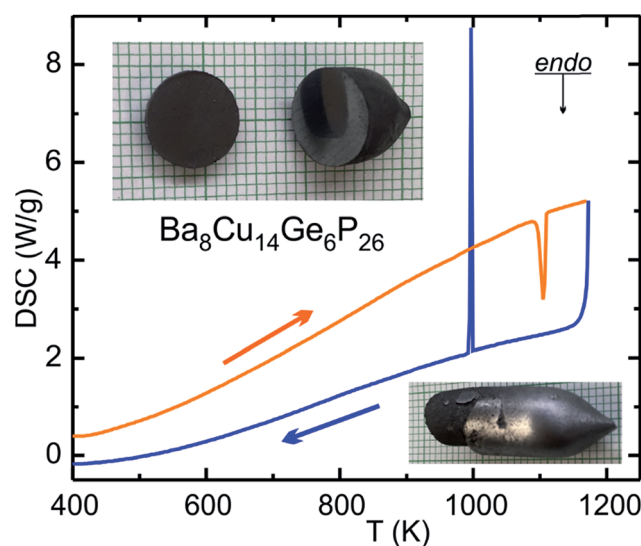

Fig. 4 DSC results for $Ba_8Cu_{14}Ge_6P_{26}$. Heating: orange curve; cooling: blue curve. The inset are photographs of (bottom) Bridgman growth crystal and (top) slices of such crystals with mirror-like surface on a background of mm-grid paper.

polycrystalline materials, the effect of grain boundaries is minimized by studying dense pellets. However, large crystals are more suitable for studying the intrinsic properties of compounds. For $Ba_8Cu_{14}Ge_6P_{26}$, characterization of slices from several crystals grown by the vertical Bridgman method were performed (Fig. 4 inset). The data obtained at UC Davis were verified by measurements at JPL. Note that JPL measurements were run on a slice of a different crystal and using different equipment (Fig. S6†). Both the low-temperature and high-temperature thermoelectric properties show good agreement with each other with small discontinuities at 300–400 K due to the different methods and instruments used (Fig. 5).

The thermopower for $Ba_8Cu_{14}Ge_6P_{26}$ samples is positive in the whole studied temperature range (10–812 K) indicating that holes are the main charge carrier type. The Seebeck thermopower was measured several times during heating and cooling in the high-temperature range with good consistency. At room temperature, a promising value for thermopower, 102 μV K^{-1}, was achieved. At the maximum measured temperature, 812 K, the thermopower value increases up to 234 μV K^{-1} (Table 2 and Fig. 5).

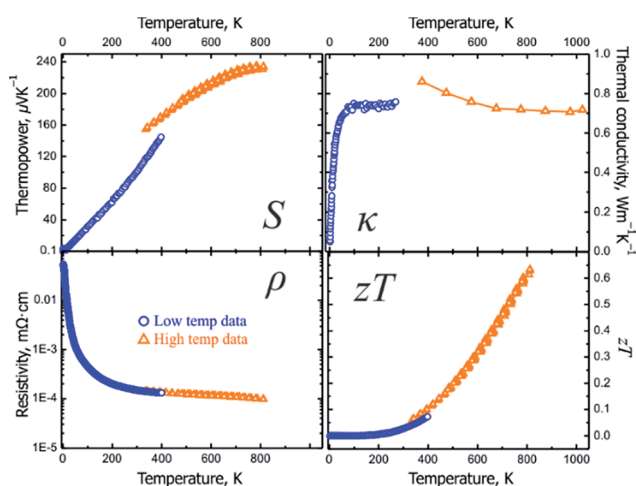**Fig. 5** Low- (blue) and high-temperature (orange) transport properties on a slice of the Bridgman growth crystal of $Ba_8Cu_{14}Ge_6P_{26}$: (top left) Seebeck thermopower; (top right) thermal conductivity; (bottom left) electrical resistivity; (bottom right) thermoelectric figure of merit, ZT. The estimated standard deviations for ZT are ~20%, see Fig. S6† and discussion therein.

$Ba_8Cu_{14}Ge_6P_{26}$ is the first quaternary anionic clathrate connecting tetrel-based and tetrel-free clathrate families. It is reasonable to compare the properties of $Ba_8Cu_{14}Ge_6P_{26}$ to the properties of its ternary counterparts, $Ba_8Cu_{5.3}Ge_{39.8}$ (ref. 46) and $Ba_8Cu_{16}P_{30}$, which are also p-type conductors. Additionally, the performance of $Ba_8Cu_{14}Ge_6P_{26}$ is compared to $Ba_8Ga_{15.8}Al_3Ge_{27}$, the one of the best performing Ge-based, p-type thermoelectric clathrate (Table 2).[47] For $Ba_8Cu_{16}P_{30}$, no high-temperature thermoelectric properties have been reported,[33] so we re-synthesized this sample and measured high-temperature thermoelectric properties shown in the last line of Table 2. The Seebeck thermopower value at 300 K of $Ba_8Cu_{14}Ge_6P_{26}$, 102 μV K^{-1}, is much higher than that for $Ba_8Cu_{16}P_{30}$ (13 μV K^{-1}) and lower than the thermopowers for $Ba_8Cu_{5.3}Ge_{39.8}$ (154 μV K^{-1}) and $Ba_8Ga_{15.8}Al_3Ge_{27}$ (187 μV K^{-1}). With increasing temperature, the Seebeck value of $Ba_8Cu_{14}Ge_6P_{26}$, 234 μV K^{-1} at 812 K, is comparable to the thermopower of the $Ba_8Ga_{15.8}Al_3Ge_{27}$ clathrate, 254 μV K^{-1} at 750 K.

The resistivities of multiple single-crystalline and pressed polycrystalline $Ba_8Cu_{14}Ge_6P_{26}$ samples decrease with increasing temperature over the whole temperature range, which indicates a thermally activated behavior typical for semiconductors (Fig. 5, bottom left). The resistivity of $Ba_8Cu_{14}Ge_6P_{26}$ at 300 K is 150 μΩ m, which decreases to 98 μΩ m at 812 K. $Ba_8Cu_{16}P_{30}$ exhibits lower resistivity, 12 μΩ m, at 300 K. In turn, the room temperature resistivity for $Ba_8Cu_{5.3}Ge_{39.8}$ is much higher, 1610 μΩ m. At 812 K, the resistivity of $Ba_8Cu_{14}Ge_6P_{26}$ remains the highest compared to the resistivities of $Ba_8Ga_{15.8}Al_3Ge_{27}$ and $Ba_8Cu_{16}P_{30}$ (Table 2). The resulting power factor for $Ba_8Cu_{14}Ge_6P_{26}$ at 812 K is 5.62 μW cm^{-1} K^{-2}. The relatively high resistivity of $Ba_8Cu_{14}Ge_6P_{26}$ indicates that further optimization of its thermoelectric efficiency can be performed via tuning the electrical conductivity by charge carrier concentration modifications. For example, for $Ba_8Ga_{16+x}Ge_{30-x}$ p-type clathrates, the typical values of ZT are less than 0.5.[48] However, a significantly higher performance was recently reported for a Bridgman growth sample with the composition $Ba_8Ga_{16.6}Ge_{28.7}$.[49] While the Seebeck coefficient and thermal conductivity for this clathrate are comparable to those of $Ba_8Cu_{14}Ge_6P_{26}$, adjustment of the Ga/Ge ratio resulted in the significant reduction of resistivity down to 35 μΩ m at 823 K.[49] Investigations of aliovalent doping into the cation sublattice of $Ba_8Cu_{14}Ge_6P_{26}$ are currently underway.

$Ba_8Cu_{14}Ge_6P_{26}$ inherits the low thermal conductivity of the clathrate family of structures due to its intrinsically complex

Table 2 A summary of the thermoelectric properties of $Ba_8Cu_{14}Ge_6P_{26}$ and related clathrates

	At 300 K				At 812 K				
	S μV K^{-1}	ρ μΩ m	κ W m^{-1} K^{-1}	ZT	S μV K^{-1}	ρ μΩ m	κ W m^{-1} K^{-1}	ZT	Ref.
$Ba_8Cu_{14}Ge_6P_{26}$	101.5	149.7	0.77	0.03	234	98	0.7	0.63	This work
$Ba_8Cu_{5.3}Ge_{39.8}$	154	1610	1.4	0.003	—	—	—	—	46
$Ba_8Ga_{15.8}Al_3Ge_{27}$[a]	187	83	1.05	0.12	254[b]	78[b]	1.0[b]	0.6[b]	47
$Ba_8Cu_{16}P_{30}$	12.8	11.7	1.2	0.004	46	19	1.4	0.07	This work

[a] $Ba_{8.01}Ga_{15.79}Al_{2.95}Ge_{26.91}$ is a p-type Ge-based clathrate with high thermoelectric performance. [b] Data at peak ZT temperature of 750 K.

host–guest structure and rattling of guest atoms.[10,16,17] The thermal conductivity of $Ba_8Cu_{14}Ge_6P_{26}$ increases with temperature and reaches a plateau at 100 K of 0.75 W m^{-1} K^{-1} without a pronounced maximum in the 50–150 K range, which is not typical for crystalline solids and more common for amorphous materials. Such behavior was observed for some clathrates with complex disorder in the framework.[16,50,51] The statistical disorder of Cu, Ge, and P seems to be responsible for such behavior and the extremely low values of the thermal conductivity for $Ba_8Cu_{14}Ge_6P_{26}$. As temperature increases, the thermal conductivity decreases down to a value of 0.72 W m^{-1} K^{-1} at 812 K. The thermal conductivity value of $Ba_8Cu_{14}Ge_6P_{26}$ is lower than the thermal conductivities of a majority of clathrate compounds (1–3 W m^{-1} K^{-1}).[16,17] The thermal conductivity of $Ba_8Cu_{14}Ge_6P_{26}$ is also comparable to that of some of the state-of-art thermoelectric materials, such as $Yb_{14}MnSb_{11}$ (0.7 W m^{-1} K^{-1} at 300 K),[52] $Bi_{0.5}Sb_{1.5}Te_3$ (0.7 W m^{-1} K^{-1} at 300 K),[53] [010] direction of the SnSe single crystal (0.7 W m^{-1} K^{-1} at 300 K),[54] and Ca_3AlSb_3 (1.3 W m^{-1} K^{-1} at 300 K).[55,56] The thermal conductivity consists of a charge carrier contribution and phonon contribution, $\kappa_{total} = \kappa_e + \kappa_L = LT/\rho + \kappa_L$ (κ_e: electronic thermal conductivity; κ_L: lattice thermal conductivity; L: Lorenz number; ρ: electrical resistivity; T: absolute temperature), where the L can be estimated based on the Seebeck coefficient values.[57] The lattice and electronic contributions to total thermal conductivity for $Ba_8Cu_{14}Ge_6P_{26}$ are shown in Fig. S5.† The lattice thermal conductivity exhibits a similar trend to the total thermal conductivity and reaches 0.58 W m^{-1} K^{-1} at 812 K, which is comparable to the lattice thermal conductivity at 800 K for many state-of-the-art thermoelectric materials, such as $Yb_{14}MnSb_{11}$ (0.51 W m^{-1} K^{-1}),[58] Sr_3GaSb_3 (0.52 W m^{-1} K^{-1}),[59] and $Ba_8Ga_{16}Ge_{30}$ (0.65 W m^{-1} K^{-1}).[60]

Finally, due to a combination of the high thermopower, ultralow thermal conductivity, and intermediate electrical conductivity, the Bridgman growth sample of $Ba_8Cu_{14}Ge_6P_{26}$ exhibits a promising thermoelectric figure of merit, ZT, of 0.63 at 812 K (Fig. 5, bottom right). The average ZT for the 400–800 K range is 0.35. The maximum ZT of $Ba_8Cu_{14}Ge_6P_{26}$ at 812 K is 9 times higher than the value for the ternary tetrel-free counterpart, $Ba_8Cu_{16}P_{30}$ (0.07). $Ba_8Cu_{14}Ge_6P_{26}$ is among the most-efficient p-type Ge-containing clathrate thermoelectrics. Compared to the highly tuned and more expensive $Ba_8Ga_{15.8}Al_3Ge_{27}$ compound, the initial achievement of ZT = 0.63 makes $Ba_8Cu_{14}Ge_6P_{26}$ an attractive platform for the development of mid- and high-temperature thermoelectrics. $Ba_8Cu_{14}Ge_6P_{26}$ exhibits comparable thermoelectric efficiency to the unoptimized $Yb_{14}MnSb_{11}$, which is the base for the development of the most efficient high-temperature p-type thermoelectric materials.[52,61–64] For example, at 812 K the thermoelectric efficiency for $Ba_8Cu_{14}Ge_6P_{26}$ and pristine $Yb_{14}MnSb_{11}$ are 0.63 and 0.53, respectively. Many strategies to tune carrier concentration and enhance electrical conductivity, such as doping,[5] band engineering,[65] and aliovalent substitutions in the framework and guest sublattices[16,17] may be applied to improve the thermoelectric efficiency of $Ba_8Cu_{14}Ge_6P_{26}$. From a chemistry point-of-view, a novel clathrate system connecting tetrel-based clathrates and tetrel-free clathrates may reinvigorate interest in searching for new clathrates with high thermoelectric performance.

Conclusions

A new clathrate compound, $Ba_8Cu_{14}Ge_6P_{26}$, was synthesized by a traditional solid-state reaction and grown as single crystal *via* the vertical Bridgman growth method. $Ba_8Cu_{14}Ge_6P_{26}$ crystallizes in a type-I clathrate structure with cubic system $Pm\bar{3}n$ space group. The three-dimensional framework is built from uniformly distributed Cu, Ge and P atoms, which is confirmed by ED, STEM, single crystal and powder synchrotron diffraction, and X-ray and neutron PDF analyses. The congruent melting of $Ba_8Cu_{14}Ge_6P_{26}$, as revealed by DSC, allows for crystal growth *via* vertical Bridgman growth, which is beneficial for exploring intrinsic physical properties. Thermoelectric characterizations show that $Ba_8Cu_{14}Ge_6P_{26}$ is a p-type semiconductor with a promising figure of merit, ZT = 0.63 at 812 K. $Ba_8Cu_{14}Ge_6P_{26}$ exhibits auspicious thermoelectric properties outperforming majority of p-type Ge-based and tetrel-free clathrates. The efforts to reduce the resistivity of $Ba_8Cu_{14}Ge_6P_{26}$ through aliovalent doping are currently underway.

Conflicts of interest

There are no conflicts to declare.

Author contributions

All authors have given approval to the final version of the manuscript.

Funding sources

Acknowledgements

References

1 T. M. Tritt, *Science*, 1996, **272**, 1276.

2 L. Bell, *Science*, 2008, **321**, 1457–1461.

3 F. J. DiSalvo, *Science*, 1999, **295**, 703–706.

4 G. J. Snyder and E. S. Toberer, *Nat. Mater.*, 2008, **7**, 105–114.

5 D. M. Rowe, *Thermoelectrics Handbook: Macro to Nano*, CRC/Taylor & Francis, Boca Raton, FL, 2006.

6 J. R. Sootsman, D. Y. Chung and M. G. Kanatzidis, *Angew. Chem., Int. Ed.*, 2009, **48**, 8616–8639.

7 G. Tan, L. D. Zhao and M. G. Kanatzidis, *Chem. Rev.*, 2016, **116**, 12123–12149.

8 J. Wang and K. Kovnir, *J. Am. Chem. Soc.*, 2015, **137**, 12474–12477.

9 J. Wang, X. C. Liu, S. Q. Xia and X. T. Tao, *J. Am. Chem. Soc.*, 2013, **135**, 11840–11848.

10 G. A. Slack, *CRC Handbook of Thermoelectrics*, ed. D. M. Rowe, CRC Press, Boca Raton, FL, 1995, p. 407.

11 M. Beekman, D. T. Morelli and G. S. Nolas, *Nat. Mater.*, 2015, **7**, 1182–1185.

12 T. Takabatake, K. Suekuni, T. Nakayama and E. Kaneshita, *Rev. Mod. Phys.*, 2014, **86**, 669.

13 C. Xiao, J. Xu, B. Cao, K. Li, M. Kong and Y. Xie, *J. Am. Chem. Soc.*, 2012, **134**, 7971–7977.

14 M. Christensen, S. Johnsena and B. B. Iversen, *Dalton Trans.*, 2010, **39**, 978–992.

15 J. Fulmer, O. I. Lebedev, V. V. Roddatis, D. Kaseman, S. Sen, J. Dolyniuk, K. Lee, A. V. Olenev and K. Kovnir, *J. Am. Chem. Soc.*, 2013, **135**, 12313–12323.

16 G. S. Nolas, *The Physics and Chemistry of Inorganic Clathrates*, Springer, Philadelphia, New York, 2014.

17 J. Dolyniuk, B. Owens-Baird, J. Wang, J. V. Zaikina and K. Kovnir, *Mater. Sci. Eng., R*, 2016, **108**, 1–46.

18 J. Dolyniuk, J. Wang, K. Lee and K. Kovnir, *Chem. Mater.*, 2015, **27**, 4476–4484.

19 S. Bobev and S. C. Sevov, *J. Solid State Chem.*, 2000, **153**, 92–105.

20 K. A. Kovnir and A. V. Shevelkov, *Russ. Chem. Rev.*, 2004, **73**, 923–938.

21 A. V. Shevelkov and K. Kovnir, *Struct. Bonding*, 2011, **139**, 97–142.

22 B. B. Iversen, A. E. C. Palmqvist, D. E. Cox, G. S. Nolas, G. D. Stucky, N. P. Blake and H. Metiu, *J. Solid State Chem.*, 2000, **149**, 455–458.

23 H. Kleinke, *Chem. Mater.*, 2010, **22**, 604–611.

24 J. Dunner and A. Mewis, *Z. Anorg. Allg. Chem.*, 1995, **621**, 191–196.

25 J. Dolyniuk, P. S. Whitfield, K. Lee, O. I. Lebedev and K. Kovnir, *Chem. Sci.*, 2017, **8**, 3650–3659.

26 J. Dolyniuk, J. V. Zaikina, D. C. Kaseman, S. Sen and K. Kovnir, *Angew. Chem., Int. Ed.*, 2017, **56**, 2418–2422.

27 *Bruker APEX2*, Bruker AXS Inc., Madison, WI, 2005.

28 G. M. Sheldrick, *Acta Crystallogr., Sect. A: Found. Crystallogr.*, 2008, **64**, 112–122.

29 T. Proffen and S. J. L. Billinge, *J. Appl. Crystallogr.*, 1999, **32**, 572–575.

30 C. L. Farrow, P. Juhas, J. W. Liu, D. Bryndin, E. S. Božin, J. Bloch, T. Proffen and S. J. L. Billinge, *J. Phys.: Condens. Matter*, 2007, **19**, 335219.

31 C. Wood, D. Zoltan and G. Stapfer, *Rev. Sci. Instrum.*, 1985, **56**, 719–722.

32 K. A. Borup, E. S. Toberer, L. D. Zoltan, G. Nakatsukasa, M. Errico, J. P. Fleurial, B. B. Iversen and G. J. Snyder, *Rev. Sci. Instrum.*, 2012, **83**, 123902.

33 D. Huo, S. Yuji Muro and T. Takabatake, *Appl. Phys. Lett.*, 2003, **82**, 2640.

34 K. Kovnir, U. Stockert, S. Budnyk, Yu. Prots, M. Baitinger, S. Paschen, A. V. Shevelkov and Y. Grin, *Inorg. Chem.*, 2011, **50**, 10387–10396.

35 M. Christensen, N. Lock, J. Overgaard and B. B. Iversen, *J. Am. Chem. Soc.*, 2006, **128**, 15657–15665.

36 S. E. Latturner, J. D. Bryan, N. Blake, H. Metiu and G. D. Stucky, *Inorg. Chem.*, 2002, **41**, 3956–3961.

37 S. Johnson, A. Bentien, G. K. H. Madsen, B. B. Iversen and M. Nygren, *Chem. Mater.*, 2006, **18**, 4633–4642.

38 J. V. Zaikina, K. A. Kovnir, U. Burkhardt, W. Schnelle, F. Haarmann, U. Schwarz, Y. Grin and A. V. Shevelkov, *Inorg. Chem.*, 2009, **48**, 3720–3730.

39 A. Kaltzoglou, T. F. Fässler, M. Christensen, S. Johnsen, B. Iversen, I. Presniakov, A. Sobolev and A. Shevelkov, *J. Mater. Chem.*, 2008, **18**, 5630–5637.

40 W. Carrillo-Cabrera, S. Budnyk, Y. Prots and Y. Grin, *Z. Anorg. Allg. Chem.*, 2004, **630**, 2267–2276.

41 F. Dubois and T. F. Fssler, *J. Am. Chem. Soc.*, 2005, **127**, 3264–3265.

42 J. V. Zaikina, K. A. Kovnir, F. Haarmann, W. Schnelle, U. Burkhardt, H. Borrmann, U. Schwarz, Y. Grin and A. V. Shevelkov, *Chem.–Eur. J.*, 2008, **14**, 5414–5422.

43 K. A. Kovnir, J. V. Zaikina, L. N. Reshetova, A. V. Olenev, E. V. Dikarev and A. V. Shevelkov, *Inorg. Chem.*, 2004, **43**, 3230–3236.

44 Y. Liu, L.-M. Wu, L.-H. Li, S.-W. Du, J. D. Corbett and L. Chen, *Angew. Chem., Int. Ed.*, 2009, **48**, 5305–5308.

45 H. He, A. Zevalkink, Z. M. Gibbs, G. J. Snyder and S. Bobev, *Chem. Mater.*, 2012, **24**, 3596–3603.

46 X. Shi, J. Yang, S. Bai, J. Yang, H. Wang, M. Chi, J. R. Salvador, W. Zhang, L. Chen and W. Wong-Ng, *Adv. Funct. Mater.*, 2010, **20**, 755–763.

47 S. Deng, X. Tang, P. Li and Q. Zhang, *J. Appl. Phys.*, 2008, **103**, 073503.

48 D. Cederkrantz, A. Saramat, G. J. Snyder and A. E. C. Palmqvist, *J. Appl. Phys.*, 2009, **106**, 074509.

49 L.-H. Wang and L.-S. Chang, *J. Alloys Compd.*, 2017, **722**, 644–650.

50 G. S. Nolas, J. L. Cohn, J. S. Dyck, C. Uher and J. Yang, *Phys. Rev. B: Condens. Matter Mater. Phys.*, 2002, **65**, 165201.

51 G. S. Nolas, B. C. Chakoumakos, B. Mahieu, G. J. Long and T. J. R. Weakley, *Chem. Mater.*, 2000, **12**, 1947–1953.

52 S. R. Brown, S. M. Kauzlarich, F. Gascoin and G. J. Snyder, *Chem. Mater.*, 2006, **18**, 1873–1877.

53 B. Poudel, Q. Hao, Y. Ma, Y. Lan, A. Minnich, B. Yu, X. Yan, D. Wang, A. Muto, D. Vashaee, X. Chen, J. Liu,

M. S. Dresselhaus, G. Chen and Z. F. Ren, *Science*, 2008, **320**, 634–638.

54 L.-D. Zhao, S.-H. Lo, Y. Zhang, H. Sun, G. J. Tan, C. Uher, C. Wolverton, V. P. Dravid and M. G. Kanatzidis, *Nature*, 2014, **508**, 373–377.

55 A. Zevalkink, E. S. Toberer, W. G. Zeier, E. Flage-Larsen and G. J. Snyder, *Energy Environ. Sci.*, 2011, **4**, 510–518.

56 W. G. Zeier, A. Zevalkink, E. Schechtel, W. Tremel and G. J. Snyder, *J. Mater. Chem.*, 2012, **22**, 9826–9830.

57 H.-S. Kim, Z. M. Gibbs, Y. Tang, H. Wang and G. J. Snyder, *APL Mater.*, 2015, **3**, 041506.

58 J.-A. Paik, E. Brandon, T. Calliat, R. Ewell and J. P. Fleurial, *Proceedings of Nuclear and Emerging Technologies for Space*, 2011.

59 A. Zevalkink, W. G. Zeier, G. Pomrehn, E. Schechtel, W. Tremel and G. J. Snyder, *Energy Environ. Sci.*, 2012, **5**, 9121–9128.

60 X. Hou, Y. Zhou, L. Wang, W. Zhang, W. Zhang and L. Chen, *J. Alloys Compd.*, 2009, **482**, 544–547.

61 E. S. Toberer, C. A. Cox, S. R. Brown, T. Ikeda, A. F. May, S. M. Kauzlarich and G. J. Snyder, *Adv. Funct. Mater.*, 2008, **18**, 2795–2800.

62 C. A. Cox, E. S. Toberer, A. A. Levchenko, S. R. Brown, G. J. Snyder, A. Navrotsky and S. M. Kauzlarich, *Chem. Mater.*, 2009, **21**, 1354–1360.

63 E. S. Toberer, S. R. Brown, T. Ikeda, S. M. Kauzlarich and G. J. Snyder, *Appl. Phys. Lett.*, 2008, **93**, 062110.

64 Y. Hu, S. K. Bux, J. H. Grebenkemper and S. M. Kauzlarich, *J. Mater. Chem. C*, 2015, **3**, 10566.

65 Y. Pei, H. Wang and G. J. Snyder, *Adv. Mater.*, 2012, **24**, 6125–6135.